

Room-temperature nonlinear transport and microwave rectification in antiferromagnetic MnBi_2Te_4 films

Shanshan Liu^{1#}, Rhonald Burgos^{2#}, Enze Zhang³, Naizhou Wang⁴, Xiao-Bin Qiang⁵, Chuanzhao Li,⁶ Qihan Zhang⁷, Z. Z. Du⁵, Rui Zheng¹, Jingsheng Chen⁷, Qing-Hua Xu¹, Kai Leng,⁶ Weibo Gao⁴, Faxian Xiu³, Dimitrie Culcer^{2*}, Kian Ping Loh^{1*}

¹Department of Chemistry, National University of Singapore, Singapore 117543, Singapore

²School of Physics, The University of New South Wales, Sydney 2052, Australia

³State Key Laboratory of Surface Physics and Department of Physics, Fudan University, Shanghai 200433, China

⁴Division of Physics and Applied Physics, School of Physical and Mathematical Sciences, Nanyang Technological University, Singapore 637371, Singapore

⁵Shenzhen Institute for Quantum Science and Engineering and Department of Physics, Southern University of Science and Technology (SUSTech), Shenzhen 518055, China.

⁶Department of Applied Physics, The Hong Kong Polytechnic University, Kowloon 999077 Hong Kong, China

⁷Department of Materials Science and Engineering, National University of Singapore, Singapore, 117575, Singapore

[#] These authors contributed equally to this work.

*Correspondence and requests for materials should be addressed to K.P.L. (Email: chmlohk@nus.edu.sg) and D.C. (Email: d.culcer@unsw.edu.au).

Abstract

The discovery of the nonlinear Hall effect provides an avenue for studying the interplay among symmetry, topology, and phase transitions, with potential applications in signal doubling and high-frequency rectification. However, practical applications require devices fabricated on large area thin film as well as room-temperature operation. Here, we demonstrate robust room-temperature nonlinear transverse response and microwave rectification in MnBi_2Te_4 films grown by molecular beam epitaxy. We observe multiple sign-reversals in the nonlinear response by tuning the chemical potential. Through theoretical analysis, we identify skew scattering and side jump, arising from extrinsic spin-orbit scattering, as the main mechanisms underlying the observed nonlinear signals. Furthermore, we demonstrate radio frequency (RF) rectification in the range of 1-8 gigahertz at 300 K. These findings not only enhance our understanding of the

relationship between nonlinear response and magnetism, but also expand the potential applications as energy harvesters and detectors in high-frequency scenarios.

Introduction

The Hall effect, which refers to the generation of a transverse voltage in response to longitudinal currents, has led to discoveries in fractional charge and statistics,^{1,2} topological phases of materials,^{3,4} and potential applications in quantum computing devices.⁵ In contrast to the linear Hall effect, where the transverse Hall voltage is linearly dependent on the longitudinal driving current, the recently identified second-order nonlinear Hall effect (NLHE) is characterized by a transverse Hall voltage that varies quadratically with the longitudinal a.c. driving currents.⁶ Moreover, NLHE occurs in systems with time-reversal symmetry,⁷ unlike the linear Hall effects that require time-reversal symmetry breaking. Various low-symmetry materials, such as atomically thin WTe₂^{8,9}, corrugated bilayer graphene¹⁰, and twisted bilayer WSe₂¹¹, exhibit Berry curvature dipole (BCD)-induced NLHE. However, BCD-induced NLHE requires stringent symmetry conditions such as the breaking of inversion and C_3 rotation symmetry,^{6,12,13} and its magnitude diminishes sharply as temperature increases due to its sensitivity to electronic band structures.^{8,9} As a result, there are only a few reports of room-temperature stable NLHE to date, as exemplified by semimetals TaIrTe₄¹⁴ and BaMnSb₂¹⁵, semiconductor BiTeBr¹², and metal Pt¹⁶. BCD-induced NLHE is predominantly a low-temperature phenomenon. Therefore, it is highly desirable to explore non-BCD-dependent mechanisms as well as materials that exhibit room-temperature nonlinear second-order effect to enable practical applications.

MnBi₂Te₄, a magnetic topological material,¹⁷⁻²¹ being the playground for studying quantum anomalous Hall effect and axion insulator states in odd/even layered devices, and nonlinear transport originating from the quantum metric dipole (QMD) has been discovered in ideal even-layer MnBi₂Te₄ devices.^{22,23} However, the QMD-induced nonlinear Hall effect disappears above the Néel temperature (\sim 23 K). In contrast, antiferromagnet CuMnAs, which possesses PT -symmetry, exhibits an intrinsic NLHE with a magnitude several orders larger, which persists above room temperature.²⁴

Although disorder effect has often been neglected in the interpretation of NLHE in *PT*-symmetric systems, recent theoretical predictions suggest that disorder can overshadow the intrinsic contribution.²⁵ In view of this, we investigate the effect of disorder on nonlinear transport by studying molecular beam epitaxy (MBE)-grown MnBi₂Te₄ films. Unlike the reported compensated antiferromagnetic (AFM) order in ideal even-layer MnBi₂Te₄ flakes, MBE-grown MnBi₂Te₄ film exhibits a net magnetization, originating from disorders.²⁶

In this study, we demonstrate the observation of nonlinear transverse response in MBE-grown MnBi₂Te₄ films that persists to 320 K. Through scaling analysis of the nonlinear transverse magnitude and longitudinal conductivity, we attribute the dominant microscopic mechanism to skew scattering and side jump effects. Unlike the quantum metric dipole mechanism observed in even-layer MnBi₂Te₄, the extrinsic spin-orbit coupling in our films introduces spin-flip scattering, an essential component of skew scattering and side jump. By tuning the gate voltage, we observe multiple sign reversals in the nonlinear transverse conductivity, with a strong dependence on the chemical potential. Leveraging this nonlinear response, MnBi₂Te₄ devices exhibit a broadband bias-free microwave rectification in the frequency range of 1-8 GHz.

Results and Discussion

Room-temperature nonlinear response in MnBi₂Te₄ films

MnBi₂Te₄ is in R $\bar{3}$ m structure with Te-Bi-Te-Mn-Te-Bi-Te septuple layer (SL), as schematically depicted in Fig. 1a. The A-type antiferromagnetic order can be described as intralayer ferromagnetic and interlayer antiferromagnetic coupling. Here, MnBi₂Te₄ films with the epitaxial orientation along the c-axis (Supplementary Fig. 1a) were directly grown on Al₂O₃ and SrTiO₃ substrates via molecular beam epitaxy.²⁶ To protect MnBi₂Te₄ from oxidation, a thin layer of 2-nm Al was grown subsequently. The layered structure with a thickness of \sim 1.39 nm was confirmed via cross-section transmission electron microscopy (TEM, Fig. 1b). We carried out the anisotropic magnetization measurements of zero-field-cooled (ZFC) and field-cooled (FC) magnetization and field-dependent magnetization along in-plane (H//ab) and out-of-

plane ($H//c$) to explore its magnetic properties. Displayed in Fig. 1c, the Néel temperature (T_N) of 20 SL $MnBi_2Te_4$ is extracted to be ~ 23 K with the ground magnetic moment along the c -axis, which is consistent with its A-type antiferromagnetic feature^{27,28}. According to the linearly polarized second harmonic generation (SHG) maps of $MnBi_2Te_4$, a six-fold pattern is present due to broken surface inversion symmetry, similar to the reported SHG of exfoliated flake²⁹. Although defects generated during the growth process may contribute to inversion symmetry breaking, such an effect is much smaller than that of the surface state-originated SHG. This is consistent with the topological insulator feature of $MnBi_2Te_4$ whose surface state has broken inversion symmetry above the Néel temperature^{17,18,30}. The intensity of the SHG varies quadratically with laser power, as displayed in Supplementary Note 2 and Fig. 2.

To perform nonlinear transport measurement, $MnBi_2Te_4$ films were fabricated into standard Hall-bar devices. The field-dependent longitudinal magnetoresistance and transverse Hall signals of 7 SL $MnBi_2Te_4$ at 2K are shown in Fig. 1e, and sheet electron carrier density can be extracted to be $2.74 \times 10^{12} \text{ cm}^{-2}$. As displayed in Fig. 1f, the anomalous Hall effect (AHE) at various temperatures can be obtained after subtracting the normal Hall part. Because of the A-type AF order with weak interlayer coupling, Mn from different layers can flip their spins independently so the multiple magnetic intermediate spin-flop states with kinks are identified in the AHE curve, which has also been observed in $MnBi_2Te_4$ bulk crystals and exfoliated nanoflake.^{18,19,31,32} Different from the exfoliated $MnBi_2Te_4$ flakes where the even-layer shows compensated antiferromagnetic order with nearly zero Hall signal at zero magnetic field,^{19,22,23} both our odd-layer and even-layer thick $MnBi_2Te_4$ films exhibit an uncompensated net magnetization with sizeable Hall signal at zero magnetic field below the Néel temperature of ~ 25 K (Fig. 1f and Supplementary Fig. 3).

Next, we examine the second harmonic signals along transverse and longitudinal directions simultaneously in Hall bar devices in which there was negligible mixing between each channel. All data were collected under zero magnetic field unless specifically mentioned. The device configuration is shown in Fig. 2a. An alternating

current $I_{//}$ ($\omega=13.7$ Hz) was applied and the voltage at the second harmonic frequency ($\omega=27.4$ Hz) was measured. We first examined the nonlinear transport in a 7 SL device (Fig. 2b), where the second harmonic transverse voltage $V_{xy}^{2\omega}$ is larger than the longitudinal voltage $V_{xx}^{2\omega}$ by 4 times. Typical curves for $V_{xy}^{2\omega}$ at 10 K and 300 K are shown in Fig. 2c. It is noteworthy that the nonlinear transverse signal can be detected at room temperature. Secondly, $V_{xy}^{2\omega}$ scales quadratically with input current, and it changes sign when the current direction and contact electrodes are inverted. The quadratic relation and sign reversal for the two opposite measurement geometries suggest its origin as a second-order nonlinear response. Figure 2d displays the temperature-dependent nonlinear second harmonic signal. As the longitudinal resistance changes with temperature, we converted the measured signal $V_{xy}^{2\omega}$ and input current $I_{//}$ to electric fields through $E_{//} = \frac{V_{//}}{L_{//}} = \frac{I_{//} \times R_{xx}}{L}$ and $E_{xy}^{2\omega} = \frac{V_{xy}^{2\omega}}{W}$ with L and W of the longitudinal length and transverse width of the device. $E_{xy}^{2\omega}$ scales linearly with $E_{//}^2$. To compare the temperature-dependent nonlinear response quantitatively, the magnitude of the nonlinear transverse response, defined as $\frac{E_{xy}^{2\omega}}{E_{//}^2}$ is used,⁹ and plotted in Fig. 2e. $\frac{E_{xy}^{2\omega}}{E_{//}^2}$ first increases as temperature increases, followed by a decreasing trend. It reaches a maximum near the critical Néel temperature of MnBi₂Te₄, which suggests the nonlinear second-order response can be used for Néel vector detection. Such a phenomenon is similar to the NLHE predicted in antiferromagnet CuMnAs.²⁴ It can be observed that the longitudinal conductivity σ_{xx} and nonlinear second-order response magnitude show similar variation with temperature (Fig. 2f).

Physical mechanism of high-temperature nonlinear response in MnBi₂Te₄

To explore the physical origin of the observed nonlinear second-order response, we study the scaling relation of the magnitude of the nonlinear second-order response $\frac{E_{xy}^{2\omega}}{E_{//}^2}$ with longitudinal conductivity σ_{xx} for devices of various thicknesses. As shown in Figs. 3a-b, the nonlinear second-order response shows a linear dependence on the

square of conductivity σ_{xx} above T_N , which is consistent with the scaling equation below

$$\frac{E_{xy}^{2\omega}}{E_{//}^2} = \xi \sigma_{xx}^2 + \eta, \quad (1)$$

where ξ and η are constants. Here, the slope ξ stands for the contribution from skew scattering effect, and the intercept η quantifies the contribution from side jump and Berry curvature dipole effects.^{9,13,33} The threefold rotation symmetry of MnBi₂Te₄ forbids in-plane Berry curvature dipole.⁷ By fitting the data, we obtain $\xi = 6.14 \times 10^{-18}$ m³V⁻¹S⁻² and $\eta = -1.81 \times 10^{-10}$ m V⁻¹ for 7 SL, which are larger than the 20 SL device ($\xi = 2.27 \times 10^{-18}$ m³V⁻¹S⁻² and $\eta = -8.76 \times 10^{-11}$ mV⁻¹ for 20 SL). This suggests that both skew scattering and side jump effects are enhanced in thinner devices, which may correlate with the bandgap difference.³⁴ The opposite sign between ξ and η indicates the competing contributions from skew scattering and side jump effects. The deviation of $\frac{E_{xy}^{2\omega}}{E_{//}^2}$ from linear scaling (values collected at around the Néel temperature) in Fig.3a may be due to the magnetic spin fluctuation³⁵. To track the symmetry-dependence of the nonlinear signal, angular-dependent measurement in a disc-like device with radially distributed electrodes was further performed. As shown in Supplementary Fig. 6b, the nonlinear second-order response shows a threefold rotational symmetry, fully compliant with the threefold symmetry of MnBi₂Te₄. Thus, the dominant mechanism is due to skew scattering and side jump effects. The extrinsic effects, like Schottky contact and Joule heating, have been safely excluded which was discussed in detail in Supplementary Note 3. Since the nonlinear conductivity $\sigma_{yxx}^{2\omega}$ can be written as: $\frac{E_{xy}^{2\omega}}{E_{//}^2} = \frac{\sigma_{yxx}^{2\omega}}{\sigma}$, the $\sigma_{yxx}^{2\omega}$ can be obtained through the experimentally determined second order response $\frac{E_{xy}^{2\omega}}{E_{//}^2}$ and conductance σ . As σ is linearly dependent on the scattering time τ , $\sigma_{yxx}^{2\omega}$ will scale with τ and τ^3 .

To gain a deeper understanding of the physical origin of the observed nonlinear transport, we consider the presence of warping in MnBi₂Te₄. The threefold rotational symmetry detected in the nonlinear transverse signals (angular dependence nonlinear

measurements displayed in Supplementary Figs. 6 and 9) suggests a hexagonal warping effect in the band structure³⁶. Additionally, an energy splitting develops between the surface states of the same band index but opposite surface momenta upon formation of the long-range magnetic order.²⁶ The effective Hamiltonian can be written as $H = H_0 + H_E + U(r)$, with the unperturbed Hamiltonian H_0 of the band Hamiltonian including hexagonal warping and a gap parameter, H_E of the external driving field and $U(r)$ for the disorder scattering potential. The unperturbed band Hamiltonian H_0 has the form

$$H_0 = H_{so} + H_w + H_m = \hbar v_F (k_x \sigma_y - k_y \sigma_x) + i \frac{\lambda}{2} (k_+^3 - k_-^3) \sigma_z + \Delta \sigma_z, \quad (2)$$

where (k_x, k_y) are the wave factors, $(\sigma_x, \sigma_y, \sigma_z)$ are the Pauli matrices, v_F is the Fermi velocity, λ is the warping parameter, Δ is the energy gap of the system, and $k_{\pm} = k_x \pm ik_y$. Here, H_{so} represents the spin-orbit coupling, H_w stems from the warping effect and H_m represents the gap. The Hamiltonian contains a tunneling (mass) term, assumed to be large, a term accounting for Rashba spin-orbit coupling which is responsible for the Dirac cone of topological insulators, as well as a warping term. The latter is vital in giving rise to a second-order response, since this requires mirror-symmetry breaking. We focus on temperatures above the Néel temperature without considering the magnetism. At these temperatures scattering arises from both phonons and impurities. Both phonons and impurities give rise to momentum scattering as well as spin-dependent scattering, which leads to spin flips. Importantly, in topological materials with strong spin-orbit interaction, the scattering potential itself contains an extrinsic spin-orbit term. Such a term is known to exist in topological insulators, where it is needed to explain the STM quasiparticle interference³⁷ and affects weak anti-localization³⁸. In our case, such an extrinsic spin-orbit term is present in the phonon as well as in the impurity scattering potentials. Determining the correct dependence and prefactors is an involving process requiring a detailed consideration of inter-band dynamics, which is sketched in Supplementary Note 1. Theoretically, we obtain the nonlinear transverse conductivity can be simplified as:

$$\sigma_{yx}^{2\omega} = \gamma_\beta (C_1 \tau_{\text{imp}} + C_2 \tau_{\text{imp}}^3) \cos 3\varphi, \quad (3)$$

where $\gamma_\beta = \beta^2 u_0^2 \pi k_F^4 \rho(\varepsilon_F) / \hbar$, φ is the angle between the current and x -axis, τ_{imp} is the momentum relaxation time. The most important findings are as follows. Firstly, both C_1 and C_2 are determined by the strength of extrinsic spin-orbit scattering and reflect the presence of both skew scattering and side jump, which are essentially indistinguishable in topological materials^{39,40}. Secondly, the joint effect of warping and the presence of a gap makes the system anisotropic⁴¹ for the observation of a nonlinear response. Thirdly, the nonlinear transverse conductivity $\sigma_{yx}^{2\omega}$ increases with increasing Fermi energy E_F , as shown in Fig. 3c. Finally, the temperature dependence is primarily due to phonon scattering, and $\sigma_{yx}^{2\omega}$ decreases with increasing temperature (Fig. 3d), since $E_F \gg k_B T$ usually for topological materials. The observed nonlinear response is a manifestation of spin-charge locking in TIs. It is well known from the Edelstein^{42,43} and spin-Hall effect^{44,45} that charge dynamics in systems with strong spin-orbit interactions affect spin dynamics. Here we see the converse effect in which spin-flip dynamics due to SOC influences charge transport. Extrinsic spin-orbit coupling is known to have a strong effect on charge transport, an example being the transition from weak localization to weak anti-localization as a function of extrinsic spin-orbit coupling strength³⁸. In our experiments, however, this effect is not related to localization, but rather to the interplay of charge and spin distributions in nonlinear response. The nonlinear second-order response $\sigma_{yx}^{2\omega}$ as a function of temperature for 7 SL and 20 SL MnBi₂Te₄ devices are shown in Fig. 3e-f, respectively. It can be fitted with the equation

$$\sigma_{yx}^{2\omega} = (1 + BT) \left[\frac{C_1}{(1+AT)} + \frac{C_2}{(1+AT)^3} \right], \quad (4)$$

where coefficient B comes from spin-orbit scattering, C_1 consists of side jump and skew scattering contributions, and C_2 stems from the skew scattering effect. By fitting the data, we obtain $B = -4.75 \times 10^{-4}$, $C_1 = 4.95 \times 10^{-14}$, and $C_2 = -4.76 \times 10^{-14}$ for 7 SL ($B = 1.59 \times 10^{-3}$, $C_1 = 6.09 \times 10^{-14}$, and $C_2 = -6.49 \times 10^{-14}$ for 20 SL). The opposite sign between ζ and η is consistent with nonlinear transverse magnitude fitting analysis (Figs. 3a-b).

The comparable value between C_1 and C_2 for each device suggests that skew scattering and side jump are on the same footing. The factor $(1+BT)$ comes from the fact that phonons also affect the skew scattering mechanism encapsulated in the extrinsic spin-orbit coupling, as shown in Supplemental S1.

According to our theoretical results in Fig. 3c, the nonlinear second-order response varies with chemical potential, thus we further investigated the $V_{xy}^{2\omega}$ as a function of gate voltage (V_g) where high-dielectric SrTiO₃ was used as a bottom gate. In Fig. 4a, $V_{xy}^{2\omega}$ presents multi oscillations and sign reversals as V_g decreasing from 140 V to -140 V, while the longitudinal resistance R_{xx} increases monotonously (Fig. 4b). The tunability of $V_{xy}^{2\omega}$ decreases with temperature (Fig. 4a), consistent with the lower R_{xx} tunability at high temperatures (Fig. 4b), which is due to the decreased dielectric constant of SrTiO₃. Two typical Hall curves at $V_g = \pm 140$ V are shown in Fig. 4c inset, whereby the negative slope suggests the Fermi energy level lies in the conduction band throughout the whole measurement. From the change of R_{xx} , we replot the V_g -dependent $V_{xy}^{2\omega}$ in the form of nonlinear transverse conductivity $\sigma_{yxx}^{2\omega}$, as displayed in Fig. 4c. The multiple sign-reversals of $\sigma_{yxx}^{2\omega}$ with chemical potential can be clearly observed. This phenomenon also helps to exclude the thermoelectric effect that only changes sign with the carrier type. Electron-dominated conduction is preserved in the whole V_g range of 160 V to -160 V with the electron density changing from 1.99×10^{13} to 5.50×10^{12} cm⁻² (Fig. 4d).

Room-temperature RF rectification in MnBi₂Te₄

The second-harmonic nonlinear response has the potential to be utilized for high-frequency rectification purposes. To test MnBi₂Te₄ device as a rectifier, we exploit its ability to perform wireless microwave rectification at room temperature, without requiring any external bias or magnetic field. As illustrated in Fig. 5a, the device is subjected to an electromagnetic wave emitted by a patch antenna. Employing the same measurement setup used for the nonlinear transport characterization, we measure the rectified DC voltage in both the transverse (V_{xy}^{dc}) and longitudinal (V_{xx}^{dc}) directions.

MnBi_2Te_4 demonstrates rectification capabilities across 1 to 8 GHz, with the best performance observed within the 1-2 GHz range, as depicted in Fig. 5b. To further illustrate the device's response, Figure 5c presents a 2D mapping of V_{xy}^{dc} as a function of RF frequency and power, demonstrating its broad bandwidth response. Figure 5d indicates that the rectification voltage V_{xy}^{dc} exhibits a linear increase with the power of the RF source. When the measurement configuration is switched to the longitudinal direction, the measured V_{xx}^{dc} also observed a linear relation with the RF power, but its magnitude is ~ 2.5 times smaller than V_{xy}^{dc} , as shown in Figs. 5e-f. Since the material can be scaled up in area via MBE growth, further improvement in rectification performance can be achieved through appropriate antenna design and optimized impedance matching circuits.

In summary, we have demonstrated a room-temperature nonlinear transverse response in topological uncompensated antiferromagnet MnBi_2Te_4 films that is independent of Berry curvature or quantum metric dipole. The quantum metric dipole previously reported for the antiferromagnet phase of MnBi_2Te_4 operates below Neel temperature^{22,23} and does not contribute to the second-order nonlinear response observed here. Instead, scaling analysis revealed that skew scattering and side jump effects associated with the anisotropic warping effect introduce the nonlinear transverse response that is robust even at room temperature. MnBi_2Te_4 can rectify broadband RF radiation over the range of 1-8 GHz without the application of external bias. Our study highlights the general contribution of warping to second-order nonlinear transport, which manifests strongly at room temperature when other intrinsic mechanisms vanish.

Methods

MnBi_2Te_4 film growth and device fabrication

MnBi_2Te_4 films on (0001) Al_2O_3 and (111) SrTiO_3 substrates were prepared by molecular beam epitaxy through the co-evaporating three fluxes of Mn, Bi, and Te.²⁶ Before taking samples out of the chamber, 2 nm Al was grown as the capping layer. The confined Hall-bar devices were fabricated by the standard electron beam lithography and reactive-ion etching processes, and Pt contacts were deposited via e-beam

evaporation.

Electrical and RF rectification measurement

The nonlinear transport measurement was performed in a Lake Shore Cryostat (CRX-VF probe station), with a Keithley 6221 source meter used to apply alternating current to MnBi_2Te_4 device and lock-in amplifiers of SR830 to collect the voltage signals. SrTiO_3 substrate served as a bottom gate with the gate voltage applied by Keithley 2636B. The magneto-transport experiment was carried out in an Oxford TeslatronPT system equipped with a multi-channel lock-in amplifier. The phases of measured first- and second-harmonic voltage are confined to $\sim 0^\circ$ and 90° , respectively. For the RF rectification measurement, an SG384 upgraded with an output frequency doubler was used to generate the RF signals ranging from 1 GHz to 8 GHz, and an antenna and Keithley 2182A nanovoltmeter were used to transmit the microwave to MnBi_2Te_4 devices and collect the rectified DC signals. The magnetization measurements were performed in DC-Superconducting-Quantum-Interface-Devices.

Data availability

Relevant data supporting the key findings of this study are available within the article and the Supplementary Information file. The raw data that support the plots within this study are available from the corresponding author upon request.

References

1. Jain, J. K. Composite-fermion approach for the fractional quantum Hall effect. *Phys. Rev. Lett.* **63**, 199–202 (1989).
2. Arovas, D., Schrieffer, J. R. & Wilczek, F. Fractional Statistics and the Quantum Hall Effect. *Phys. Rev. Lett.* **53**, 722–723 (1984).
3. Niu, Q., Thouless, D. J. & Wu, Y.-S. Quantized Hall conductance as a topological invariant. *Phys. Rev. B* **31**, 3372–3377 (1985).
4. Thouless, D. J., Kohmoto, M., Nightingale, M. P. & den Nijs, M. Quantized Hall Conductance in a Two-Dimensional Periodic Potential. *Phys. Rev. Lett.* **49**, 405–408 (1982).
5. Nayak, C., Simon, S. H., Stern, A., Freedman, M. & Das Sarma, S. Non-Abelian anyons and topological quantum computation. *Rev. Mod. Phys.* **80**, 1083–1159 (2008).
6. Du, Z. Z., Lu, H.-Z. & Xie, X. C. Nonlinear Hall effects. *Nat. Rev. Phys.* **3**, 744–752 (2021).
7. Sodemann, I. & Fu, L. Quantum Nonlinear Hall Effect Induced by Berry Curvature Dipole in Time-Reversal Invariant Materials. *Phys. Rev. Lett.* **115**, 216806 (2015).
8. Ma, Q. *et al.* Observation of the nonlinear Hall effect under time-reversal-symmetric conditions. *Nature* **565**, 337–342 (2019).
9. Kang, K., Li, T., Sohn, E., Shan, J. & Mak, K. F. Nonlinear anomalous Hall effect in few-layer WTe₂. *Nat. Mater.* **18**, 324–328 (2019).
10. Ho, S.-C. *et al.* Hall effects in artificially corrugated bilayer graphene without breaking time-reversal symmetry. *Nat. Electron.* **4**, 116–125 (2021).
11. Huang, M. *et al.* Giant nonlinear Hall effect in twisted bilayer WSe₂. *Natl. Sci. Rev.* **10**, nwac232 (2023).
12. Lu, X. F. *et al.* Nonlinear transport and radio frequency rectification in BiTeBr at room temperature. *Nat. Commun.* **15**, 245 (2024).
13. He, P. *et al.* Quantum frequency doubling in the topological insulator Bi₂Se₃. *Nat. Commun.* **12**, 698 (2021).
14. Kumar, D. *et al.* Room-temperature nonlinear Hall effect and wireless radiofrequency rectification in Weyl semimetal TaIrTe₄. *Nat. Nanotechnol.* **16**, 421–425 (2021).
15. Min, L. *et al.* Strong room-temperature bulk nonlinear Hall effect in a spin-valley locked Dirac material. *Nat. Commun.* **14**, 364 (2023).

16. Min, L. *et al.* Colossal nonreciprocal Hall effect and broadband frequency mixing due to a room temperature nonlinear Hall effect. Preprint at <https://doi.org/10.48550/arXiv.2303.03738> (2023).
17. Li, J. *et al.* Intrinsic magnetic topological insulators in van der Waals layered MnBi₂Te₄-family materials. *Sci. Adv.* **5**, eaaw5685 (2019).
18. Otkrov, M. M. *et al.* Prediction and observation of an antiferromagnetic topological insulator. *Nature* **576**, 416–422 (2019).
19. Deng, Y. *et al.* Quantum anomalous Hall effect in intrinsic magnetic topological insulator MnBi₂Te₄. *Science* **367**, 895–900 (2020).
20. Ge, J. *et al.* High-Chern-number and high-temperature quantum Hall effect without Landau levels. *Natl. Sci. Rev.* **7**, 1280–1287 (2020).
21. Liu, C. *et al.* Robust axion insulator and Chern insulator phases in a two-dimensional antiferromagnetic topological insulator. *Nat. Mater.* **19**, 522–527 (2020).
22. Gao, A. *et al.* Quantum metric nonlinear Hall effect in a topological antiferromagnetic heterostructure. *Science* **381**, 181–186 (2023).
23. Wang, N. *et al.* Quantum-metric-induced nonlinear transport in a topological antiferromagnet. *Nature* **621**, 487–492 (2023).
24. Wang, C., Gao, Y. & Xiao, D. Intrinsic Nonlinear Hall Effect in Antiferromagnetic Tetragonal CuMnAs. *Phys. Rev. Lett.* **127**, 277201 (2021).
25. Atencia, R. B., Xiao, D. & Culcer, D. Disorder in the nonlinear anomalous Hall effect of PT-symmetric Dirac fermions. *Phys. Rev. B* **108**, L201115 (2023).
26. Liu, S. *et al.* Gate-tunable Intrinsic Anomalous Hall Effect in Epitaxial MnBi₂Te₄ Films. *Nano Lett.* **24**, 16–25 (2024).
27. Cui, J. *et al.* Transport properties of thin flakes of the antiferromagnetic topological insulator MnBi₂Te₄. *Phys. Rev. B* **99**, 155125 (2019).
28. Zeugner, A. *et al.* Chemical Aspects of the Candidate Antiferromagnetic Topological Insulator MnBi₂Te₄. *Chem. Mater.* **31**, 2795–2806 (2019).
29. Fonseca, J. *et al.* Anomalous Second Harmonic Generation from Atomically Thin MnBi₂Te₄. *Nano Lett.* **22**, 10134–10139 (2022).
30. Chen, Y. J. *et al.* Topological Electronic Structure and Its Temperature Evolution in Antiferromagnetic Topological Insulator MnBi₂Te₄. *Phys. Rev. X* **9**, 041040 (2019).
31. Yang, S. *et al.* Odd-Even Layer-Number Effect and Layer-Dependent Magnetic Phase Diagrams in MnBi₂Te₄. *Phys. Rev. X* **11**, 011003 (2021).
32. Ovchinnikov, D. *et al.* Intertwined Topological and Magnetic Orders in Atomically Thin Chern Insulator MnBi₂Te₄. *Nano Lett.* **21**, 2544–2550 (2021).
33. Du, Z. Z., Wang, C. M., Li, S., Lu, H.-Z. & Xie, X. C. Disorder-induced nonlinear Hall effect with time-reversal symmetry. *Nat. Commun.* **10**, 3047 (2019).
34. Otkrov, M. M. *et al.* Unique Thickness-Dependent Properties of the van der Waals Interlayer Antiferromagnet MnBi₂Te₄ Films. *Phys. Rev. Lett.* **122**, 107202 (2019).
35. Lujan, D. *et al.* Magnons and magnetic fluctuations in atomically thin MnBi₂Te₄. *Nat. Commun.* **13**, 2527 (2022).
36. Fu, L. Hexagonal Warping Effects in the Surface States of the Topological Insulator Bi₂Te₃. *Phys. Rev. Lett.* **103**, 266801 (2009).
37. Lee, W.-C., Wu, C., Arovas, D. P. & Zhang, S.-C. Quasiparticle interference on the surface of the topological insulator Bi₂Te₃. *Phys. Rev. B* **80**, 245439 (2009).
38. Adroguer, P., Liu, W. E., Culcer, D. & Hankiewicz, E. M. Conductivity corrections for topological insulators with spin-orbit impurities: Hikami-Larkin-Nagaoka formula revisited. *Phys. Rev. B* **92**, 241402 (2015).
39. Atencia, R. B., Niu, Q. & Culcer, D. Semiclassical response of disordered conductors: Extrinsic carrier velocity and spin and field-corrected collision integral. *Phys. Rev. Res.* **4**, 013001 (2022).
40. Sinitzyn, N. A. Semiclassical theories of the anomalous Hall effect. *J. Phys. Condens. Matter* **20**, 023201 (2007).
41. Naselli, G. *et al.* Magnetic warping in topological insulators. *Phys. Rev. Res.* **4**, 033198 (2022).
42. Edelstein, V. M. Spin polarization of conduction electrons induced by electric current in two-dimensional asymmetric electron systems. *Solid State Commun.* **73**, 233–235 (1990).
43. Aronov, A. G., LYANDA-GELLER, YU. B., PIKUS, G. E & PARSONS, D. Spin polarization of electrons by an electric current. *J. Exp. Theor. Phys.* **73**, 537–541 (1991).

44. Sinova, J., Valenzuela, S. O., Wunderlich, J., Back, C. H. & Jungwirth, T. Spin Hall effects. *Rev. Mod. Phys.* **87**, 1213–1260 (2015).
45. Murakami, S. Quantum Spin Hall Effect and Enhanced Magnetic Response by Spin-Orbit Coupling. *Phys. Rev. Lett.* **97**, 236805 (2006).
46. Ma, Q. *et al.* Observation of the nonlinear Hall effect under time-reversal-symmetric conditions. *Nature* **565**, 337–342 (2019).
47. Qin, M.-S. *et al.* Strain Tunable Berry Curvature Dipole, Orbital Magnetization and Nonlinear Hall Effect in WSe₂ Monolayer*. *Chin. Phys. Lett.* **38**, 017301 (2021).
48. Shvetsov, O. O., Esin, V. D., Timonina, A. V., Kolesnikov, N. N. & Deviatov, E. V. Nonlinear Hall Effect in Three-Dimensional Weyl and Dirac Semimetals. *JETP Lett.* **109**, 715–721 (2019).
49. Dzsaber, S. *et al.* Giant spontaneous Hall effect in a nonmagnetic Weyl–Kondo semimetal. *Proc. Natl. Acad. Sci.* **118**, e2013386118 (2021).
50. Tiwari, A. *et al.* Giant c-axis nonlinear anomalous Hall effect in Td-MoTe₂ and WTe₂. *Nat. Commun.* **12**, 2049 (2021).
51. Ma, T. *et al.* Growth of bilayer MoTe₂ single crystals with strong non-linear Hall effect. *Nat. Commun.* **13**, 5465 (2022).
52. Kiswandhi, A. & Osada, T. Observation of possible nonlinear anomalous Hall effect in organic two-dimensional Dirac fermion system. *J. Phys. Condens. Matter* **34**, 105602 (2021).
53. He, P. *et al.* Graphene moiré superlattices with giant quantum nonlinearity of chiral Bloch electrons. *Nat. Nanotechnol.* **17**, 378–383 (2022).

Acknowledgments

K.P.L. acknowledges the support from Singapore's National Research Foundation, Prime Minister's Office, Singapore under Competitive Research Program Award NRF-CRP22-2019-0006. F.X. was supported by the National Natural Science Foundation of China (52350001, 52225207, and 11934005), the Shanghai Pilot Program for Basic Research - FuDan University 21TQ1400100 (21TQ006), and the Shanghai Municipal Science and Technology Major Project (Grant No.2019SHZDZX01).

Author contributions

K.P.L. conceived and supervised the project. S.L. fabricated the devices and performed the transport measurement. Q.Z. and J.C. performed the magnetization measurement. C.L., R.Z., Q.X., and K.L. performed the SHG measurement. N.W. and S.L. measured the RF rectification under the supervision of W.G.. S.L., X.-B.Q., Z.Z.D, and K.P.L. analyzed the data. R.B. and D.C. performed the theoretical calculations. E.Z. and F.X. grew the MnBi₂Te₄ films. S.L., R.B., D.C., and K.P.L. wrote the manuscript, with input from all authors.

Ethics declarations

Competing interests

The authors declare no competing interests.

Figure captions

Fig. 1 | Atomic structure and basic characterization of schematic picture of MnBi₂Te₄. **a**, Crystal structure from side view (top) and top view (bottom). **b**, Cross-section high-resolution transmission electron microscopy. The layer thickness is extracted to be ~ 1.39 nm. Scale bar: 1 nm. **c**, Zero-field-cooled (ZFC) and field-cooled (FC) magnetization along c-axis and ab-plane. The Néel temperature (T_N) is estimated to be ~ 23 K. The applied magnetic field is 5000 Oe. Inset, Magnetization hysteresis along the c-axis and ab-plane measured at 1.8 K. **d**, Polar-plot of second harmonic generation (SHG) data at 300 K, represented by black dots, confirming the broken surface inversion symmetry. The red dash lines are fitting to the equation in J.F. et.al²⁹. **e**, Longitudinal magnetoresistance (R_{xx}) and Hall data (R_{xy}) under out-of-plane magnetic field measured at 2 K. The inset is the measurement configuration with in-plane current I and out-of-plane magnetic field $\mu_0\mathbf{H}$. **f**, Anomalous Hall data (R_{AHE}) at different temperatures. Multiple spin-flop steps originate from the A-type antiferromagnetism.

Fig. 2 | Observation of room-temperature nonlinear second-order response in 7 septuple layer (SL) MnBi₂Te₄. **a**, Schematic geometry of the nonlinear transport measurement. Gold, blue, and brown elements indicate the Pt contact, MnBi₂Te₄ sample, and Al₂O₃ substrate, respectively. **b**, Second harmonic nonlinear response along transverse ($V_{xy}^{2\omega}$) and longitudinal direction ($V_{xx}^{2\omega}$). The inset indicates the measurement configuration. **c**, $V_{xy}^{2\omega}$ as a function of current. Dash lines are the quadratic fittings. $V_{xy}^{2\omega}$ depends quadratically on the current and changes sign when the current direction reverses. The insets indicate the different measurement configurations. **d**, Typical temperature-dependent $E_{xy}^{2\omega}$ versus $E_{//}^2$. $E_{xy}^{2\omega}$ shows a linear dependence on $E_{//}^2$ in the measured temperature range of 10 K-310 K. **e**, The magnitude of nonlinear transverse response $\frac{E_{xy}^{2\omega}}{E_{//}^2}$ as a function of temperature. The error bars are added based on the standard fitting error of $E_{xy}^{2\omega}$ versus $E_{//}^2$. **f**, Temperature-dependent longitudinal conductivity.

Fig. 3 | Scaling of the nonlinear second-order response with longitudinal conductivity. Magnitude of nonlinear transverse response $\frac{E_{xy}^{2\omega}}{E_{//}^2}$ as a function of the square of conductivity σ_{xx}^2 for **a**, 7 SL and **b**, 20 SL MnBi₂Te₄ devices. The error bars are added based on the standard fitting error of $E_{xy}^{2\omega}$ versus $E_{//}^2$. **c**, The calculated

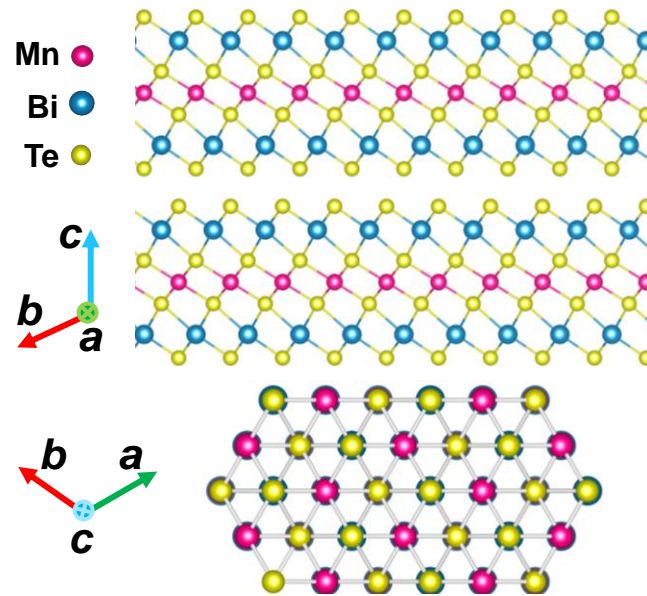
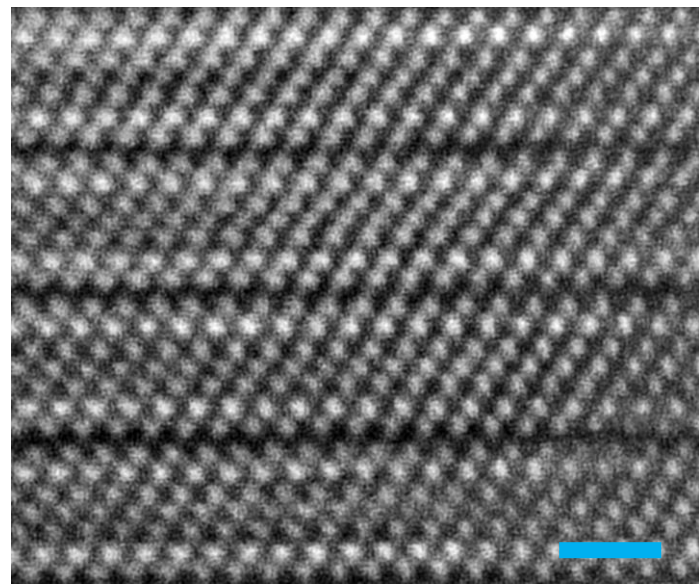
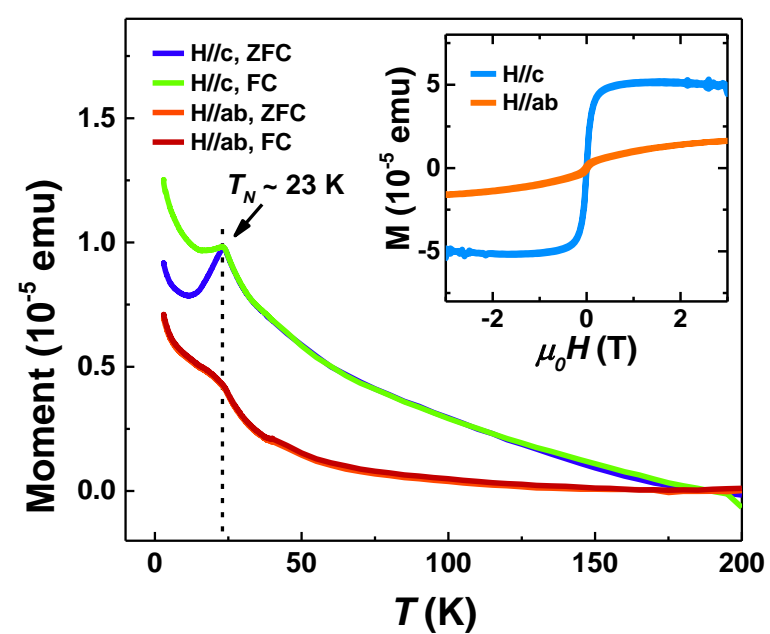
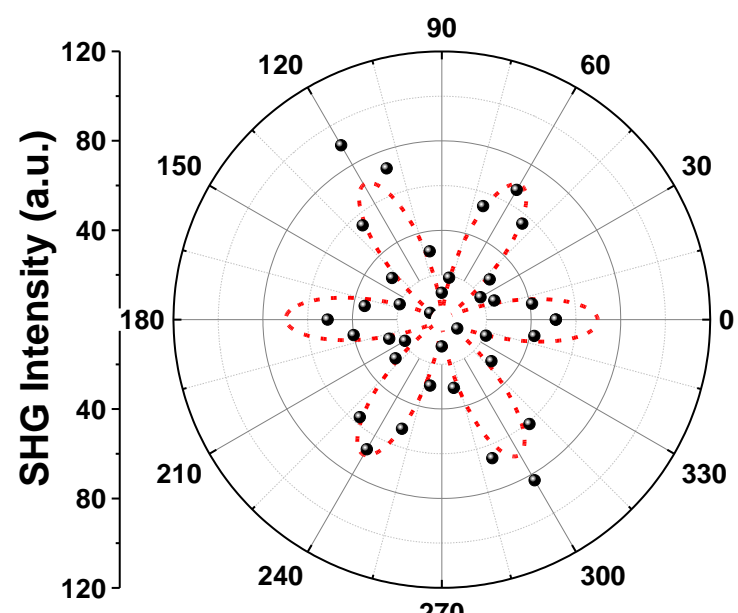
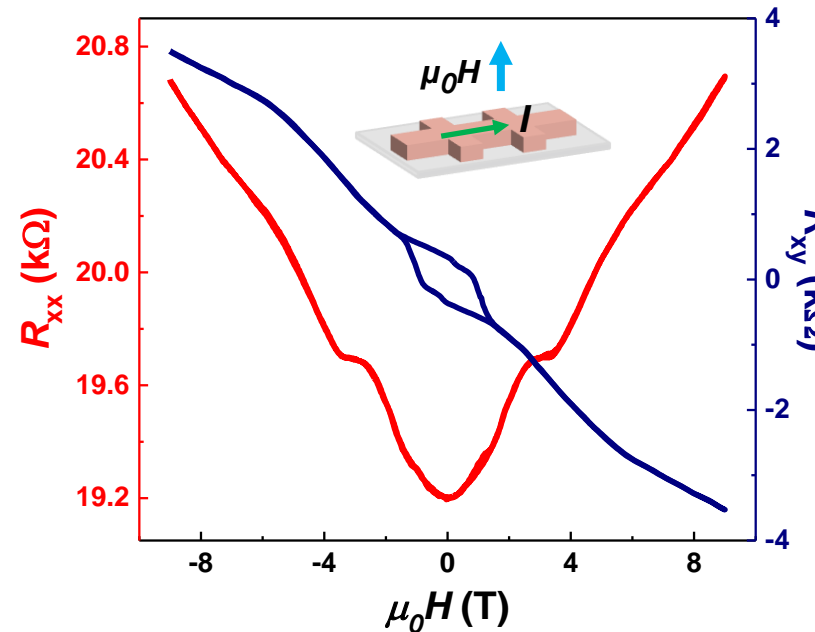
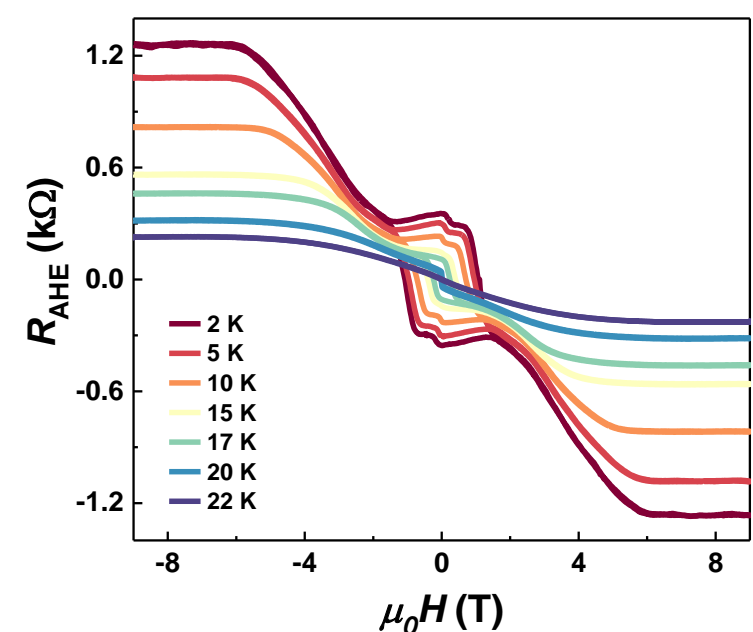
nonlinear transverse conductivity ($\sigma_{yx}^{2\omega}$) as a function of Fermi energy (E_F) for bandgap $\Delta=15$ meV, 20 meV and 25 meV at zero temperature. We take the Fermi velocity $v_F=1.6\times 10^5$ m/s, the warping constant $\lambda=80$ eVÅ³, impurity relaxation time $\tau_{\text{imp}}=0.12$ ps and scattering time $1/\gamma_\beta=0.12$ ps. **d**, The calculated $\sigma_{yx}^{2\omega}$ as a function of temperature for impurity relaxation time $\tau_{\text{imp}}=0.12$ ps, 0.125 ps and 0.13 ps. Here, Fermi energy, bandgap, and scattering time $1/\gamma_\beta$ are fixed to be 25 meV, 15 meV and 1.2 ps, respectively. **e, f**, Temperature-dependent $\sigma_{yx}^{2\omega}$ for 7 SL and 20 SL devices. The dash lines are the theoretical fitting results. The error bars are added based on the standard fitting error of $E_{xy}^{2\omega}$ versus $E_{//}^2$.

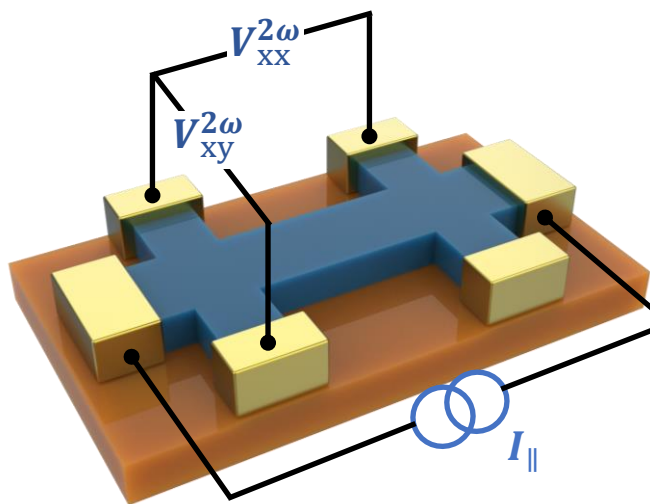
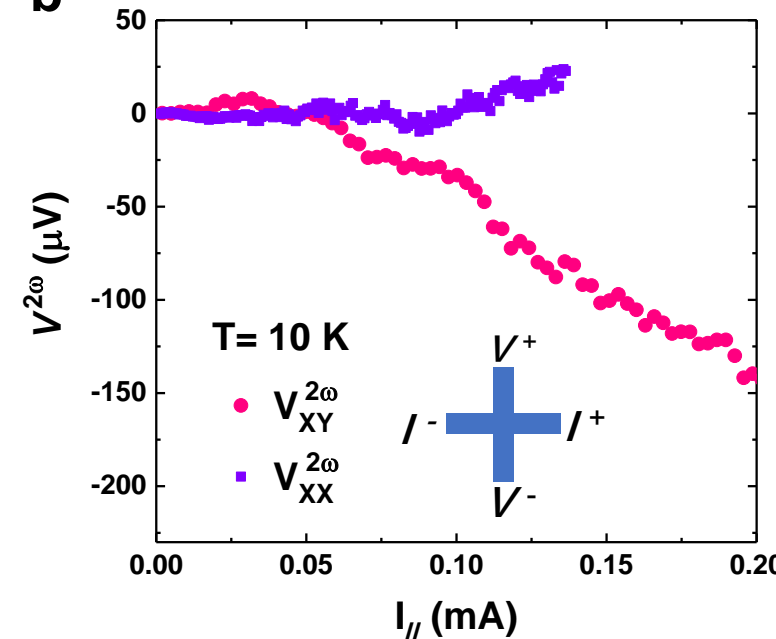
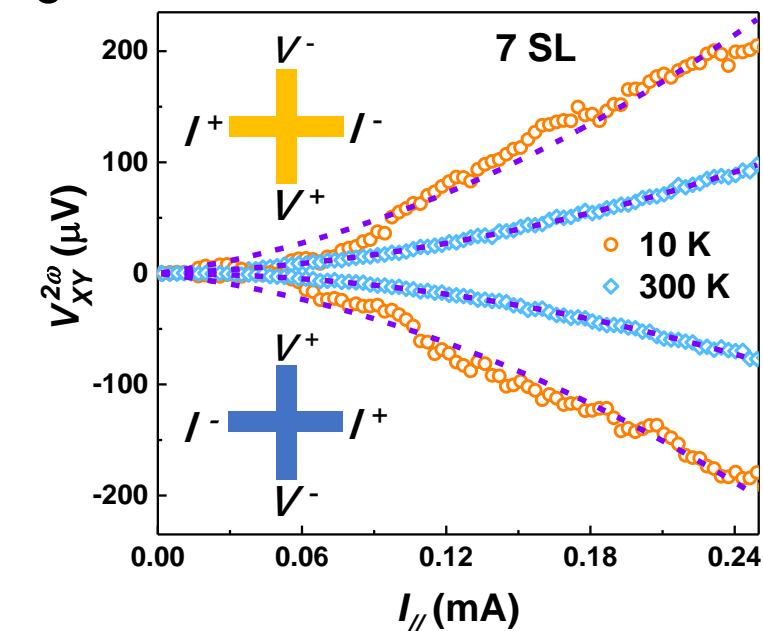
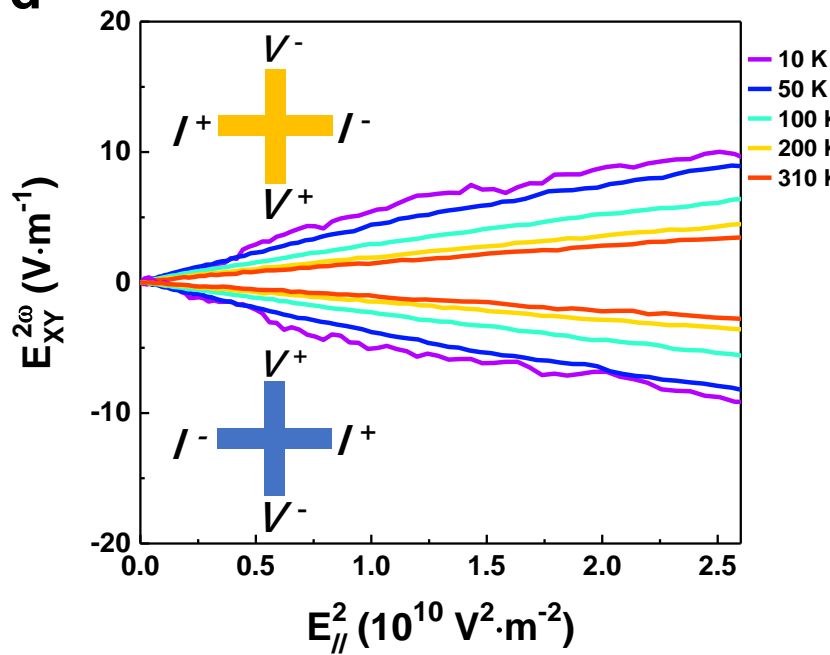
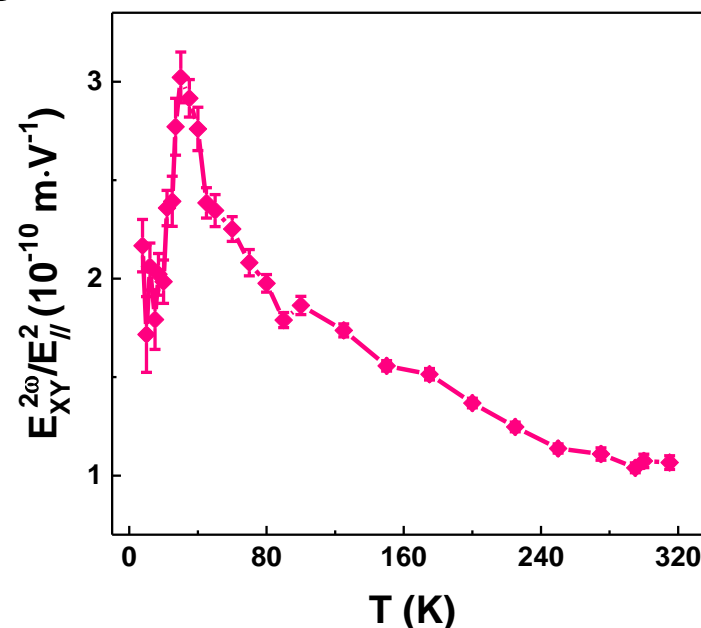
Fig. 4 | Gate-tunable nonlinear transport. **a**, Second harmonic nonlinear response along transverse ($V_{xy}^{2\omega}$) a function of gate voltage (V_g). **b**, The longitudinal resistance (R_{xx}) as a function of V_g . Inset, typical Hall data under $V_g=\pm 140$ V. The sample shows electron-dominated conduction property in the whole applied V_g . **c**, The corresponding nonlinear transverse conductivity $\sigma_{yx}^{2\omega}$ as a function of V_g , with multiple sign-reversal. This helps to exclude the thermoelectric effect. **d**, Electron carrier density (n) and mobility (μ) as a function of V_g measured at 7.6 K. The error bars are added based on the standard fitting error of Hall data at different V_g .

Fig. 5 | Room-temperature wireless rectification. **a**, Schematic illustration of rectification measurement on MnBi₂Te₄ device. **b**, The rectified DC voltage along the transverse direction (V_{xy}^{dc}). It shows a broad response among 1-8 GHz. **c**, 2D mapping plot of rectification signal as a function of power (P_{IN}) and frequency (f_{IN}). The highest V_{xy}^{dc} corresponds to the frequency of 1.7 GHz. **d**, V_{xy}^{dc} as a function of the radiofrequency power. **e**, The rectified DC voltage along the longitudinal direction (V_{xx}^{dc}). **f**, V_{xx}^{dc} versus radio frequency power.

Table 1 The second-harmonic nonlinear signal in different materials

Materials	Input current maximum (μA)	Output voltage maximum (μV)	Highest working temperature (K)	References
Bilayer WTe ₂	1	200	100	Ref. ⁴⁶
Few-layer WTe ₂	600	30	100	Ref. ⁹
Strained monolayer WSe ₂	4.5	20	140	Ref. ⁴⁷
Twisted bilayer WSe ₂	0.04	20,000	30	Ref. ¹¹
Corrugated bilayer graphene	0.1	2	15	Ref. ¹⁰
Bi ₂ Se ₃	1,500	20	200	Ref. ¹³
Bulk WTe ₂	110	4,000	4.2	Ref. ⁴⁸
Cd ₃ As ₂	110	4,000	4.2	Ref. ⁴⁸
Ce ₃ Bi ₄ Pd ₃	10,000	0.8	4	Ref. ⁴⁹
T _d -MoTe ₂ (c-axis)	5,000	40	40	Ref. ⁵⁰
T _d -MoTe ₂ (in-plane)	97	125	100	Ref. ⁵¹
TaIrTe ₄	600	120	300	Ref. ¹⁴
α-(BEDT-TTF) ₂ I ₃	1,000	9	40	Ref. ⁵²
Pt	50	120	375	Ref. ¹⁶
hBN/graphene/hBN moiré superlattice	5	100	220	Ref. ⁵³
4SL MnBi ₂ Te ₄ flake	10	200	20	Ref. ²³
6SL MnBi ₂ Te ₄ /BP heterostructure	10	350	20	Ref. ²²
BaMnSb ₂	100	250	400	Ref. ¹⁵
BiTeBr	5	100	>350	Ref. ¹²
MnBi ₂ Te ₄ films	250	225	>320	This work

a**b****c****d****e****f**

a**b****c****d****e****f**